J Nanostruct 16(1): 691-698, Winter 2026

RESEARCH PAPER

Self-Powered $Cd_{1-x}Cu_xS$/n-Si Nanocomposite Heterojunction Photodetectors with Enhanced Optoelectronic Response

Zaid Mohammed Jasima, Nahida B. Hasana, Mohsin K. Al-khaykaneea*

Department of Physics, College of Science, University of Babylon, Iraq

ARTICLE INFO

Article History:
Received 19 September 2025
Accepted 28 December 2025
Published 01 January 2026

Keywords:
AACVD
Hexagonal crystal system
Nanocomposite
Photodetector

ABSTRACT

In this work, $Cd_{1-x}Cu_xS$ (x = 0, 0.25, 0.5, 0.75, 1) thin films were deposited on n-Si substrates using aerosol-assisted chemical vapor deposition (AACVD). The films, with an average thickness of 350 ± 10 nm, were investigated to correlate their structural and optical properties with photodetector performance. X-ray diffraction (XRD) confirmed the formation of a pure crystalline phase with a well-ordered lattice. UV-Vis spectroscopy revealed strong absorption in the visible and UV regions, essential for photodetection applications. The fabricated photodetector demonstrated light absorption and emission at specific wavelengths, which can be attributed to electronic transitions within the crystal structure. The $Cd_{1-x}Cu_xS$/n-Si heterojunction photodetectors exhibited high photoresponsivity (≈0. 306 A/W at 620 nm) and fast response times (<0.34 s), demonstrating efficient charge transfer and suppressed recombination. The enhanced crystallinity further facilitated charge transport, reducing energy loss and improving sensitivity. These findings highlight AACVD-grown $Cd_{1-x}Cu_xS$ as a promising material system for cost-effective, high-performance optoelectronic devices.

How to cite this article
Jasima Z., Hasana N., Al-khaykaneea M. Self-Powered $Cd_{1-x}Cu_xS$/n-Si Nanocomposite Heterojunction Photodetectors with Enhanced Optoelectronic Response. J Nanostruct, 2026; 16(1):691-698. DOI: 10.22052/JNS.2026.01.062

INTRODUCTION

Thin films of semiconductor compounds represent a significant research topic in the fields of energy, electronics, and photonics, owing to their unique physical and chemical properties. Among these compounds, cadmium-copper sulfide (CdCuS) has been receiving increasing attention due to its exceptional optical and electronic characteristics, making it a promising candidate for applications such as solar cells [1], sensors [2], and microelectronic components [3]. The combination of cadmium (Cd) and copper (Cu) with sulfur (S) in a single crystal structure imparts unique electronic properties to the compound, including a tunable bandgap, efficient light absorption in the visible spectrum, and good electrical conductivity.Deposition methods for this material, such as chemical bath deposition (CBD) and spray pyrolysis, play a crucial role in determining its structure and properties [4]. CdCuS combines the properties of cadmium sulfide (CdS) and copper sulfide (CuS), allowing for enhanced optical and electrical characteristics of the resulting films through the control of elemental ratios, synthesis conditions, and deposition techniques [5]. Aerosol-assisted chemical vapor deposition (AACVD) is one of the leading techniques used for the fabrication of thin films

* *Corresponding Author Email: Zaid543X21@gmail.com*

and functional coatings, especially in applications related to energy, electronics, and optics [6]. This method involves generating an aerosol from a solution of chemical precursors typically using an ultrasonic atomizer or compressed air which is then transported to a heated zone. In this zone, the precursors decompose and deposit onto the substrate surface, forming a thin film [6]. AACVD offers several advantages over conventional deposition techniques, including the use of non-volatile precursors and the precise control of film structure, porosity, and chemical composition [7]. Additionally, it allows for the deposition of films on large or non-uniform substrates, making it suitable for a wide range of applications, such as solar cells, sensors, smart windows, and optical components [9].

MATERIALS AND METHODS

$Cd_{1-x}Cu_xS$ thin films were deposited onto n-Si and glass substrates using the aerosol-assisted chemical vapor deposition (AACVD) technique. The chemical precursors cadmium chloride monohydrate ($CdCl_2{\cdot}H_2O$), copper (II) chloride dihydrate ($CuCl_2{\cdot}H_2O$), and thiourea (CH_4N_2S) were used without further purification. The deposition system consisted of an ultrasonic nebulizer that generated an aerosol from the precursor solution and directed it into a heated glass reaction chamber. Cleaned glass substrates were placed on a heated substrate holder maintained at 300 °C ± 20 °C. The aerosolized precursor solution was carried into the chamber, where deposition occurred over duration of 45 minutes. Afterward, Substrates were allowed to cool naturally to room temperature. For n-Si <111> substrates, a diluted hydrofluoric acid (HF) solution (1:10 with deionized water) was used to remove the native SiO_2 layer prior to deposition. The substrates were then rinsed and dried before being placed into the deposition system. The composition of the deposited films was controlled by varying the precursor ratios, as shown in Table 1, which presents the specific volumes used to prepare different $Cd_{1-x}Cu_xS$ compositions. The structural properties were analyzed using a PANalytical Aeris X-ray diffractometer (XRD). Optical characteristics were examined with a Shimadzu UV-1900 spectrophotometer. Gold electrodes were deposited on both sides of the $Cd_{1-x}Cu_xS$/n-Si substrate using a sputtering-based electrode deposition system. Time-dependent photo-switching behavior was investigated using LEDs emitting light at specific wavelengths: blue (460 nm), green (550 nm), and red (620 nm). The corresponding light intensities were 5.61 mW/cm² for blue, 10.38 mW/cm² for green, and 5.11 mW/cm² for red. All measurements were performed at room temperature without applying an external voltage.

RESULTS AND DISCUSSION

Structural properties

The XRD patterns of ($Cd_{1-x}Cu_xS$) in Fig. 1 show that the films exhibit a polycrystalline structure. The XRD peaks are slightly shifted from the positions given in the ICDD card. The interplanar spacing (d_{hkl}) was determined using Bragg's law [10].

$$m\lambda = 2\, d_{hk1} \sin\theta \quad (1)$$

From Fig. 1, when x = 0 (pure CdS sample), three peaks appear which can be attributed to the (111), (220), and (311) planes of the cubic CdS phase. For the cubic structure with lattice constants a = b = c = 5.78641 Å (JCPDS #00-101-1251), when x = 1 (pure CuS film), four diffraction peaks were observed corresponding to the (002), (103), (106), and ($\bar{2}$10) planes of the hexagonal CuS phase, with lattice constants a = b = 3.77668 Å and c = 16.09649 Å (JCPDS #00-101-0920), which agrees with [4]. The

Table1. Shows the volumes of precursor solutions used to prepare the $Cd_{1-x}Cu_xS$ films.

Ratio (x)	0.05 M CH_4N_2S (ml)	0.05M $CdCl_2{\cdot}H_2O$ (ml)	0.05 M $CuCl_2{\cdot}H_2O$ (ml)
1	50	0	50
0.75	50	12.5	37.5
0.5	50	25	25
0.25	50	37.5	12.5
0	50	500	0

effect of the mixing ratio on the crystal structure appears clearly with the incorporation of Cu, as slight shifts in peak positions and reductions in intensity were observed. Moreover, the single diffraction peak seen in CuS disappears at approximately 2θ = 11°.

Table 2 presents the computed values for several parameters, including interplanar spacing (dhkl) crystallite size (D), dislocation density (δ), and internal lattice strain (ε). The X-ray diffraction patterns of the films show that the interplanar distances did not change significantly; however, they slightly decreased proportionally with increasing x.

The lattice constant (a) for CdS was calculated from the (111), (220), and (311) planes using Eq. 2 [10].

$$\frac{1}{d_{hkl}^2} = \frac{h^2 + k^2 + l^2}{a^2} \quad (2)$$

Similarly, for CuS, the lattice constant (a) was calculated from the (Ƶ10) plane, and the lattice constant (c) was obtained from the (002) plane using Eq. 3 [10].

$$\frac{1}{d_{hkl}^2} = \frac{4}{3}\left(\frac{h^2 + hk + k^2}{a^2}\right) + \frac{l^2}{c^2} \quad (3)$$

The preferred orientations of the CuS film were found to be associated with the hexagonal structure (where a = b ≠ c). These orientations also change with the addition of Cd, confirming that mixing with CdS affects the crystal structure of the ($Cd_{1-x}Cu_xS$) films.

The Scherrer formula was used to estimate the crystallite size (D) using Eq. 4 [10]. The crystallite size was found to decrease with increasing x, as shown in Table 2.

$$D = \frac{0.94\lambda}{\beta \cos\theta} \quad (4)$$

Lattice deformation microstrain (ε›) and dislocation density (δ), based on the Williamson–Smallman method, were calculated using Eqs. 5 and 6, respectively [11]. It was observed that both microstrain (ε›) and dislocation density (δ) increase as the crystallite size (D) decreases.

$$\varepsilon' = \frac{\beta \cos\theta}{4} \quad (5)$$

$$\delta = \frac{1}{D^2} \quad (6)$$

Where β is the full width at half maximum (FWHM) of the peak, λ is the wavelength of the

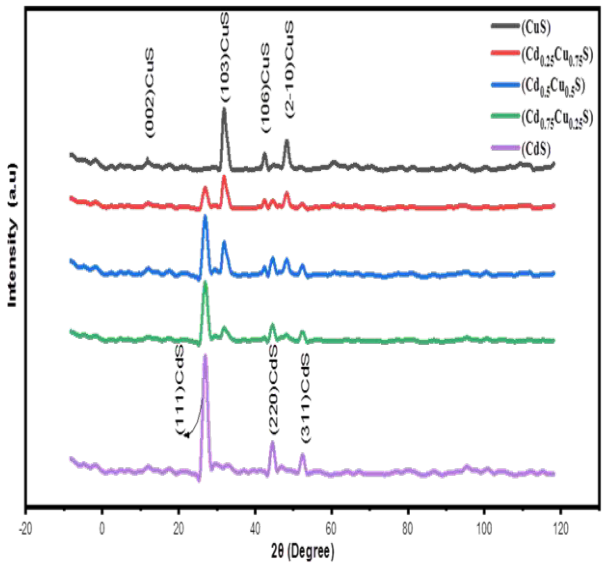

Fig. 1. X-ray diffraction patterns of the prepared ($Cd_{1-x}Cu_xS$) films at different volume percentages of x.

incident X-ray, and θ is the Bragg diffraction angle.

Optical properties

Fig. 2 shows the absorption spectra of ($Cd_{1-x}Cu_xS$) films. The films exhibit a distinctive absorbance around 350 nm. It is evident that the absorbance decreases with increasing wavelength, but increases with higher x values. On the other hand, the absorbance becomes nearly constant at wavelengths above 600 nm. This behavior indicates that the incorporation of Cu into the CdS matrix enhances the absorption in the UV–visible region due to the narrowing of the optical band gap and the increased density of localized states. The increased Cu content introduces addi-tional energy levels within the band structure, which facilitates more photon absorption, particularly at shorter wavelengths. This makes the material more suitable for optoelectronic and photovoltaic applications, as it allows better utilization of the solar spectrum.

Electrical properties

Sensitivity (S) is used to evaluate the increase in current in a sample under illumination. The conductivity increases when the light is turned on, and once the light is turned off, the current returns to its original value. This cycle is repeated multiple times to verify the stability of the device's photo response. Figs. 3– illustrate the current–time (I–t) characteristics of the photodetector device under illumination and in the dark (ON and OFF states), highlighting the rise and fall times in each case. The measurements were performed at wavelengths of 460 nm, 520 nm, and 620 nm, in the absence of an external bias voltage. The sensitivity values corresponding to the applied wavelengths were calculated using Eq. 7 [12].

$$S = \left(\frac{I_{phot} - I_{dark}}{I_{dark}}\right) \times 100 \quad (7)$$

Eq. 8 [13] describes the responsivity of photodiodes, which relates the output photocurrent to the incident optical power, denoted as Pin. The calculated responsivity values are listed in Table 3. The responsivity of the fabricated devices varies with the x ratio for all applied wavelengths. This variation may be attributed to changes in the number of free carriers contributing to the recorded current.

$$R_\lambda = \frac{I_{photo}}{P_{in} S} \quad (8)$$

Table2. X-ray diffraction parameters of ($Cd_{1-x}Cu_xS$) films at different volume percentages.

Ratio x	2θ (deg)	(d) nm	FWHM (β) deg	G. S nm	strain (ε') nm	(δ) nm^{-2}
0	26.7	0.33408	0.43	18.9817	0.00183	0.00277544
	44.43	0.20402	0.489	17.5416	0.00198	0.00324982
	52.3	0.17502	0.57	15.5199	0.00223	0.00415165
0.25	26.8	0.33285	0.46	17.7474	0.00195	0.0031749
	32.7	0.27402	0.43	19.2468	0.0018	0.00269949
	42.37	0.21345	0.331	25.7305	0.00135	0.00151045
	44.47	0.20385	0.493	17.4018	0.00199	0.00330226
	48.29	0.18858	0.379	22.9614	0.00151	0.00189672
	52.32	0.17496	0.574	15.4131	0.00225	0.0042094
0.5	26.85	0.33225	0.47	17.3716	0.00199	0.00331375
	32.35	0.27691	0.423	19.5479	0.00177	0.00261697
	42.31	0.21374	0.322	26.4443	0.00131	0.00143
	44.55	0.2035	0.502	17.0947	0.00203	0.00342198
	48.26	0.18869	0.372	23.3907	0.00148	0.00182774
	52.38	0.17477	0.581	15.2313	0.00227	0.00431048
0.75	26.93	0.33128	0.475	17.1916	0.00202	0.0033835
	32.12	0.27884	0.414	19.9613	0.00174	0.0025097
	42.34	0.2136	0.316	26.9491	0.00129	0.00137693
	44.61	0.20324	0.51	16.8301	0.00206	0.0035304
	48.22	0.18883	0.356	24.4382	0.00142	0.00167442
	52.49	0.17443	0.593	14.9301	0.00232	0.00448613
1	11	0.804824	0.25	31.9138	0.00108	0.000981839
	31.9	0.28071	0.4	20.6486	0.00168	0.00234541
	42.3	0.21379	0.3	28.3826	0.00122	0.00124136
	48.2	0.18891	0.35	24.8552	0.00139	0.0016187

The generation and movement of electron–hole pairs are the primary factors determining the responsivity of a junction, which is considered one of its most important characteristics. Another key parameter is the external quantum efficiency (EQE), which provides insight into the accumulation of photogenerated charge carriers resulting from the absorption of a single photon. The efficiency of optical-to-electrical (O/E) conversion can be evaluated using EQE. The quantum efficiency values (η) are closely related to the spectral response and were calculated using Eq. 9 [14].

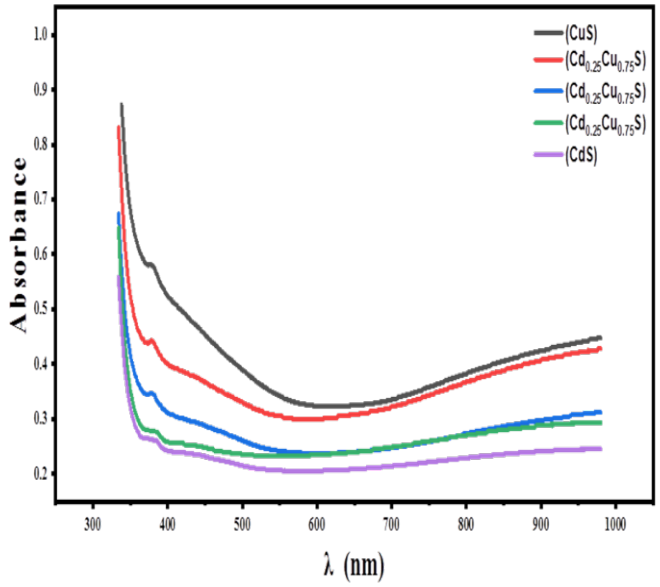

Fig. 2. Absorbance spectra as a function of wavelength for ($Cd_{1-x}Cu_xS$) films at different volume percentages of x.

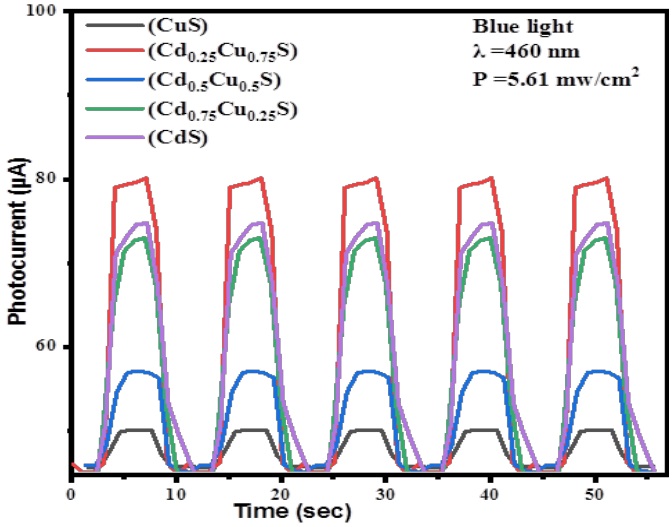

Fig. 3. The variation of photocurrent with time for ($Cd_{1-x}Cu_xS$)/n-Si self-powered photodetectors under illumination at a wavelength of 460 nm and light intensity of 5.61 mW/cm² is investigated.

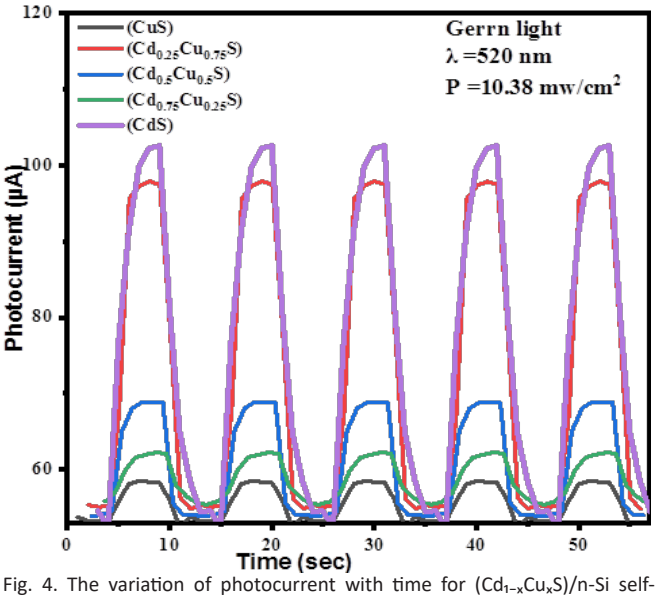

Fig. 4. The variation of photocurrent with time for $(Cd_{1-x}Cu_xS)$/n-Si self-powered photodetectors under illumination at a wavelength of 520 nm and light intensity of 10.38 mW/cm² is investigated.

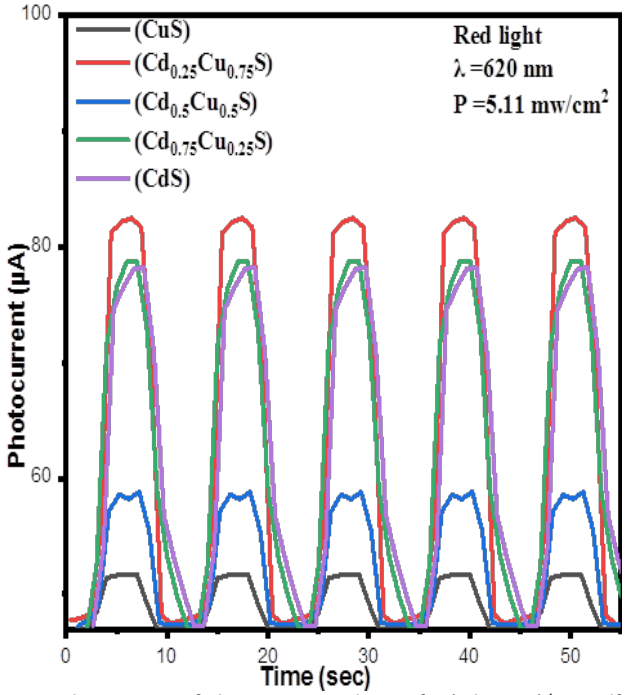

Fig. 5. The variation of photocurrent with time for $(Cd_{1-x}Cu_xS)$/n-Si self-powered photodetectors under illumination at a wavelength of 620 nm and light intensity of 5.11 mW/cm² is investigated.

Table3. Summarizes the key figures of merit for the photodetectors, including responsivity, noise-equivalent power (NEP), quantum efficiency (η), and specific detectivity (D*), under illumination at wavelengths of 460 nm, 520 nm, and 620 nm.

Ratio x	S %	$R_\lambda \times 10^{-3}$ A/W	η(λ)%	NEP×10^{-14}W.$Hz^{1/2}$	D*×10^{13}(cm.$Hz^{1/2}$.W^{-1})	(D) ×10^{13} (W. $Hz^{1/2}$)$^{-1}$
			Blue light (460 nm)			
1	5.217391	57.51633987	15.50440466	6.23974	5.47402	1.60263
0.75	17.23108	279.7385621	75.4077863	2.9709	11.1904	3.36599
0.5	12.22222	120.0237671	32.35423287	5.84027	6.42812	1.71225
0.25	21.51899	228.1639929	61.50507634	6.58402	10.2622	1.51883
0	18	210.3386809	56.69999225	5.7724	9.48864	1.73238
			Green light (520 nm)			
1	3.250478	34.68208092	8.270342374	17.5128	0.245076	0.571011
0.75	19.70443	156.0693642	37.21654068	8.92752	0.604941	1.12013
0.5	16.85393	66.79511882	15.9280668	11.148	0.360529	0.897021
0.25	4.145078	129.0944123	30.78405217	15.9285	0.493396	0.627805
0	32.67974	130.3789338	31.09036115	8.27638	0.583644	1.20826
			Red light (620 nm)			
1	10.86957	66.53620352	13.3072407	6.5333	0.508862	1.53062
0.75	16.91542	306.5883888	61.31767776	5.12157	1.18514	1.95253
0.5	12.22222	131.7677756	26.35355512	6.10898	0.715228	1.63693
0.25	81.5534	243.9660796	48.79321592	6.37539	1.0598	1.56853
0	18.66667	232.2243966	46.44487932	5.24397	1.04448	1.90695

$$EQE = R_\lambda \times \frac{hc}{q\lambda} \times 100\% \quad (9)$$

The noise equivalent power (NEP) in photoconductive detectors is determined using Equation (10) [15]. The minimum NEP value for the $Cd_{0.25}Cu_{0.75}S$ /n-Si photodetector was found to be (2.9709×10^{-14}W W/$Hz^{0.5}$) at 460 nm, which is consistent with the spectral responsivity results. This indicates that maximum responsivity is achieved when the detector's noise level is minimized.

$$NEP = i_n/R_\lambda \quad (10)$$

The specific detectivity (D*) of a photodetector refers to its ability to detect low-intensity optical signals. It is a critical parameter that combines the detector's sensitivity and noise characteristics, allowing for the comparison of performance across different devices. Specific detectivity is calculated using the Eqs. 11 and 12 [16]:

$$f = \frac{0.35}{\tau_r} \quad (11)$$

$$D = \frac{1}{NEP} \quad (12)$$

Where: f is the electrical bandwidth of the detector, τ_r is the rise time of the device, D is the general detectivity, S is the effective area of the detector, NEP is the noise equivalent power. Using Eq. 13 [16], the specific detectivity (D*) was calculated for the fabricated devices.

$$D^* = \frac{\sqrt{Sf}}{NEP} \quad (13)$$

The specific detectivity (D*) of the fabricated $Cd_{1-x}Cu_xS$/n-Si photodetectors exhibited significant enhancement across different wavelengths. The highest D* value of 11.1904× 10^{13} cm·$Hz^{1/2}$·W^{-1} was observed under blue light (460 nm) at x = 0.75, while the lowest value of 0.245076× 10^{13} cm·$Hz^{1/2}$·W^{-1} occurred at x = 1. For green light (520 nm), the maximum D* reached 0.604941× 10^{13} at x = 0.75, whereas under red light (620 nm), the peak value was 1.18514× 10^{13} at x = 0.75. This improvement correlates with a reduction in noise equivalent power (NEP), which reached 2.9709× 10^{-14} W·$Hz^{1/2}$ at x = 0.75. These results confirm the enhanced sensitivity and low-noise performance of the devices, particularly at optimized Cu concentrations, making them promising candidates for low-power photodetection applications.

CONCLUSION

The XRD results revealed that the deposited material exhibited a well-defined crystalline

structure, as evidenced by the presence of sharp diffraction peaks, indicating high crystallinity. The appearance of broad peaks in some regions may suggest the presence of nanoparticles or internal lattice strain.

The variation in grain size is likely to influence the optical properties, particularly by enhancing absorbance in the UV–Visible region. These findings confirm that the Aerosol-Assisted Chemical Vapor Deposition (AACVD) method is effective in producing thin films with promising structural and optical characteristics. Furthermore, the process shows potential for further optimization by adjusting deposition parameters to better understand the correlation between structure and device performance. The XRD and UV–Vis absorbance results also indicate that the AACVD-grown films were homogeneous and exhibited good adhesion to the substrate.

ACKNOWLEDGMENT

The authors are deeply indebted to the administration of the Department of Physics, College of Science, University of Babylon, Iraq.

CONFLICT OF INTEREST

The authors declare that there is no conflict of interests regarding the publication of this manuscript.

REFERENCES

1. Kéomany D, Poinsignon C, Deroo D. Sol gel preparation of mixed cerium—titanium oxide thin films. Sol Energy Mater Sol Cells. 1994;33(4):429-441.
2. Gannouni M, Kanzari M. Erratum to "Structural, optical and electrical properties of CuIn5S8 thin films grown by thermal evaporation method" [J. Alloys Compd. 509 (2011) 6004–6008]. J Alloys Compd. 2011;509(30):7998-8000.
3. Kim KM, Tampo H, Shibata H, Niki S. Growth and characterization of coevaporated Cu2SnSe3 thin films for photovoltaic applications. Thin Solid Films. 2013;536:111-114.
4. Ashok Kumar M, Muthukumaran S. Effect of deposition time on structural, optical and photoluminescence properties of $Cd_{0.9}Zn_{0.1}S$ thin films by chemical bath deposition method. Journal of Materials Science: Materials in Electronics. 2013;24(8):2858-2865.
5. Mahadik MA, Hunge YM, Shinde SS, Rajpure KY, Bhosale CH. Semiconducting properties of aluminum-doped ZnO thin films grown by spray pyrolysis technique. Journal of Semiconductors. 2015;36(3):033002.
6. Naik AJT, Bowman C, Panjwani N, Warwick MEA, Binions R. Electric field assisted aerosol assisted chemical vapour deposition of nanostructured metal oxide thin films. Thin Solid Films. 2013;544:452-456.
7. Binions R, Carmalt CJ, Parkin IP. Aerosol-assisted chemical vapour deposition of sodium fluoride thin films. Thin Solid Films. 2004;469-470:416-419.
8. Chem. Vap. Deposition (10–11–12/2014). Chem Vap Deposition. 2014;20(10-11-12).
9. Jassim ZM, Shiaa SAOAL. Fabrication NiO: Cu / Si Heterojunction by the Aerosol-Assisted Chemical Vapor Deposition (AACVD). Neuroquantology. 2021;19(4):57-64.
10. Khan MAM, Khan W. Thickness-Dependent Structural and Optoelectronic Properties of In_2O_3 Films Prepared by Spray Pyrolysis Technique. J Electron Mater. 2016;45(8):4453-4459.
11. Chand S, Kumar S, Sharma AK, Singh KN. Metal-Free Decarboxylative Cyanomethylation of β-Aryl/Heteroaryl Substituted α,β-Unsaturated Carboxylic Acids to γ-Ketonitriles. Org Lett. 2024;26(46):10051-10055.
12. Liang GX, Li CH, Zhao J, Fu Y, Yu ZX, Zheng ZH, et al. Self-powered broadband kesterite photodetector with ultrahigh specific detectivity for weak light applications. SusMat. 2023;3(5):682-696.
13. Punde AL, Shah SP, Hase YV, Waghmare AD, Shinde PS, Bade BR, et al. Self-biased photodetector using 2D layered bismuth triiodide (BiI_3) prepared using the spin coating method. RSC Advances. 2022;12(46):30157-30166.
14. Huo N, Konstantatos G. Recent Progress and Future Prospects of 2D-Based Photodetectors. Adv Mater. 2018;30(51).
15. Jiang M, Zhang J, Yang W, Wu D, Zhao Y, Wu Y, et al. Flexible Self-Powered Photoelectrochemical Photodetector with Ultrahigh Detectivity, Ultraviolet/Visible Reject Ratio, Stability, and a Quasi-Invisible Functionality Based on Lift-Off Vertical (Al,Ga)N Nanowires. Advanced Materials Interfaces. 2022;9(16).
16. AlSultani MJ, Alias MF. Enhanced optoelectronics performance of hybrid self power photodetectors GO: TiO_2-AD / n-Si heterojunctions. Karbala International Journal of Modern Science. 2024;10(3).